SOFT ROBOTS

MXene artificial muscles based on ionically cross-linked $Ti_3C_2T_x$ electrode for kinetic soft robotics

Sima Umrao, Rassoul Tabassian, Jaehwan Kim, Van Hiep Nguyen, Qitao Zhou, Sanghee Nam, Il-Kwon Oh*

Existing ionic artificial muscles still require a technology breakthrough for much faster response speed, higher bending strain, and longer durability. Here, we report an MXene artificial muscle based on ionically cross-linked $Ti_3C_2T_x$ with poly(3,4 ethylenedioxythiophene)-poly(styrenesulfonate), showing ultrafast rise time of within 1 s in DC responses, extremely large bending strain up to 1.37% in very low input voltage regime (0.1 to 1 V), long-term cyclic stability of 97% up to 18,000 cycles, markedly reduced phase delay, and very broad frequency bandwidth up to 20 Hz with good structural reliability without delamination under continuous electrical stimuli. These artificial muscles were successfully applied to make an origami-inspired narcissus flower robot as a wearable brooch and dancing butterflies and leaves on a tree as a kinetic art piece. These successful demonstrations elucidate the wide potential of MXene-based soft actuators for the next-generation soft robotic devices including wearable electronics and kinetic art pieces.

INTRODUCTION

The past several decades in the fields of bioinspired and biomimetic technology have seen electroactive polymer (EAP) actuators receive enormous interest as artificial muscles for use in soft robotics, wearable touch-feedback systems, stretchable and flexible electronics, and microelectromechanical systems (*1*–*3*). Among EAP actuators, ionic polymer-metal composite actuators have emerged as one of the most attractive EAP actuators due to their light weight, superior performance, air-working stability under low driving voltage, and ease of fabrication at low cost (*2*, *4*–*6*). The electrochemical strain of air-working ionic soft (AWIS) actuators depends on storing electrical energy in a double interface and converting it to mechanical energy by reversible migration of ion intercalation and de-intercalation at the interface of the electrode and the electrolyte membrane and in the electrode (*7*).

However, for AWIS actuators, the essential requirements are a considerable bending strain, fast response time, low driving voltage, and high durability in the air. Conducting electrodes are critical components in AWIS actuators, covering the two opposite faces of the ionic polymer membrane. These electrodes must be compatible and compliant with the ionic polymer membrane during bending and must maintain their electrical conductivity and high capacitance. As far as electrode materials are concerned, carbon-based materials, because of their high theoretical capacity, are attracting extensive attention for AWIS actuators (*2*, *4*, *8*–*20*). Recently, several approaches using nanomaterials or designing nano-architectures with enhanced electrochemical properties or charge storage/transport mechanisms have been developed for next-generation high-performance AWIS actuators. For example, millimeter-long single-walled carbon nanotube (CNT)–based actuators have exhibited high strain (*21*); three-dimensional (3D) nanocarbon electrodes (reduced graphene oxide–CNTs) with highly stable porous networks showed promising cycling stability (1 million cycles) in electrochemical actuators (*22*). 3D graphitic carbon nitride and nitrogen-doped graphene heteronanostructure-based AWIS actuator electrodes were found to exhibit bending strain (0.52%) at low frequency (0.1 Hz) with 93% actuation retention (*4*), and a graphdiyne-based actuator showed promising electromechanical transduction efficiency of up to 6.03% with 0.8% bending strain (*16*). However, the sluggish kinetics of large-size ionic-liquid cations, poor transport, severe lack of intercalated ions, and high response time during conversion reaction lead to poor rate capacities under high frequency. These limitations mainly arise from sluggish insertion/extraction and diffusion of ionic liquid ions at the interface of the polymer membrane and across the conducting electrode (*18*). Therefore, new electrode materials that can exceed the requirements of next-generation AWIS actuators are strongly required.

Newly discovered materials under the broad title MXene are part of a young family of 2D transition metal carbides and/or nitrides with the formula $M_{n+1}X_nT_x$, where M represents an early transition metal (e.g., Ti, Zr, V, Nb, Ta, or Mo); X represents carbon and/or nitrogen; T_x represents the number of surface terminations, such as O, OH, and/or F; and $n = 1, 2$, or 3. They are very promising candidates for energy storage devices, transparent conductive electrodes, electromagnetic interference shielding, etc. (*23*–*29*). Among more than 20 different types of MXene, $Ti_3C_2T_x$ has been the most studied variety of MXene to date because of its metal-like conductivity and high storage capacity. Interlayer spacing of $Ti_3C_2T_x$ can be changed via intercalation and de-intercalation of ions (K^+, Mg^{2+}, Na^+, etc.) (*30*). Thus, $Ti_3C_2T_x$ is a good candidate electrode material for AWIS actuators.

However, because of the lack of stretchability of MXene, it is difficult to fabricate surface-agnostic MXene coating, which could have good adhesion to polymer electrolyte layers and withstand extreme mechanical deformation. Thus far, for flexible energy storage and electrode applications, $Ti_3C_2T_x$ composites with various polymers—such as sodium alginate (*27*), polyvinyl alcohol (*31*), polypyrrole (*32*), and polydiallyldimethylammonium chloride (*31*)—have been developed with high tensile strength but with a compromise on conductivity. Therefore, conducting polymers should be polymeric matrices that can maintain the conductivity and act as a binder to

Creative Research Initiative Center for Functionally Antagonistic Nano-Engineering, Department of Mechanical Engineering, Korea Advanced Institute of Science and Technology (KAIST), 291 Daehak-ro, Yuseong-gu, Daejeon 34141, Republic of Korea.
*Corresponding author. Email: ikoh@kaist.ac.kr

enhance the mechanical strength of $Ti_3C_2T_x$. A previous study developed $Mo_{1.33}C$–poly(3,4 ethylenedioxythiophene) (PEDOT)–poly(styrenesulfonate) (PSS) (PP) composites based on ultrathin flexible solid-state supercapacitors that showed a higher capacitance (1310 F cm^{-3}) (*24*) because of a synergistic effect of increased interlayer spacing between $Mo_{1.33}C$ MXene layers due to insertion of conductive PEDOT and surface redox processes of PEDOT and MXene. PP has been studied as a conducting electrode material for use in AWIS actuators; however, it exhibits high response time and low bending strain because of its low capacitance (*33*). Because of the hydrophilic nature of PP when coupled with active and charged surface groups (such as $-SO_3H$ and $-SO_3^-$), PP is a potentially ideal candidate for polymeric matrices for $Ti_3C_2T_x$; also, PEDOT molecules have a positive surface, which can electrostatically interact with the negatively charged surface of $Ti_3C_2T_x$. To date, no ionically cross-linked form of MXene with a polymer has been reported as an electrode for AWIS actuators.

Here, we report MXene-based AWIS actuators and their soft robotic applications to kinetic art pieces. Simultaneous intercalation and self-assembly of PP chains ionically bonded with $Ti_3C_2T_x$ provide a synergistically favorable architecture for fast charge transport and ion intercalation/de-intercalation, resulting in exceptionally high actuation performance compared with those characteristics of neat PP and neat $Ti_3C_2T_x$. Ionically cross-linked $Ti_3C_2T_x$ exhibited not only remarkable improvement of high bending strain ~1.37% without any signs of back-relaxation but also excellent cycling stability (more than 18,000 cycles), strong blocking forces, and highly durable stability for several weeks. We successfully applied our actuator for a narcissus-inspired kinetic robot controlled by electric signals as a wearable brooch. In addition, we successfully demonstrated dancing leaves and butterflies on a tree as kinetic art soft robots by using the MXene-based AWIS actuator.

RESULTS

Structure and chemical characterizations of ionically cross-linked $Ti_3C_2T_x$ MXene

$Ti_3C_2T_x$ MXene was prepared using LiF with HCl for selective etching of Al atoms out of MAX phase Ti_3AlC_2 (see Materials and Methods and fig. S1). The crystal structure of layered $Ti_3C_2T_x$ was terminated by T_x (—OH, —O, and —F) on two surfaces. Figure 1A schematically illustrates the procedures for preparing the ionically cross-linked $Ti_3C_2T_x$-PP electrodes and fabricating the AWIS actuators (see details in Materials and Methods). Briefly, the delaminated $Ti_3C_2T_x$ suspension was mixed with PP at two different ratios, 1:4 and 1:2, of $Ti_3C_2T_x$:PP. Schematic representation of the layered structure of MXene ionically cross-linked with PP is displayed in Fig. 1A and fig. S2A. The transmission electron microscopy (TEM) image (fig. S1B) shows a few layers of $Ti_3C_2T_x$ sheets. The high-resolution TEM image (fig. S1C) shows lattice fringes that further confirm the high-level crystallinity of MXene; the interlayer spacing corresponding to the (002) plane is 0.91 nm. A scanning electron microscopy (SEM) image shows the several-micrometer nacre-like layered stacking of exfoliated $Ti_3C_2T_x$ MXene (Fig. 1B). SEM images of the 1:2 ratio $Ti_3C_2T_x$-PP are shown in Fig. 1C and indicate that nacre-like layered stacking of $Ti_3C_2T_x$ remains, with large interlayer spacing, because of the construction of interlayer support of PP due to the high electrostatic/ionic attraction. Further, Raman spectroscopy was used to understand the molecular-level interaction that occurred between $Ti_3C_2T_x$ and PP. Figure 1D shows representative bands of $Ti_3C_2T_x$ in the range of 150 to 750 cm^{-1}. The Raman $\omega_{1g}(E_g)$ mode of about 166 cm^{-1} at room temperature mainly corresponds to the in-plane vibrations of Ti2 and C atoms (*34*). The Raman modes at 200 and 689 cm^{-1} correspond to out-of-plane stretching vibrations of Ti, C, and O atoms (*34*). Another Raman mode was attributed to

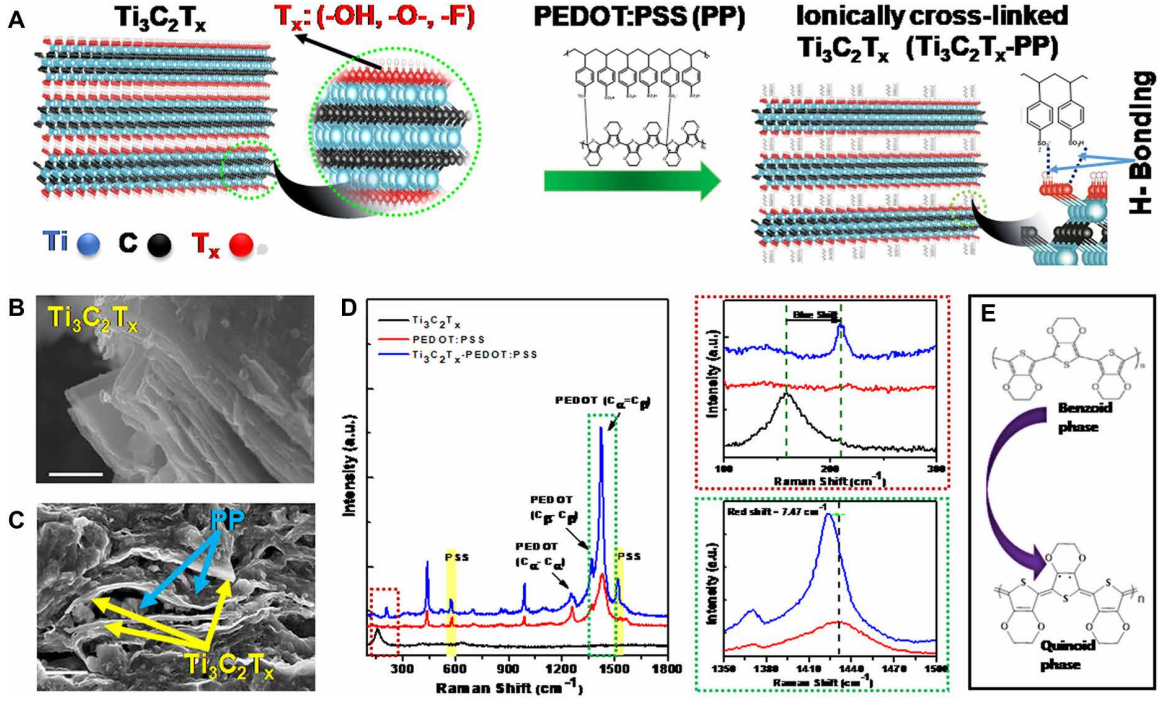

Fig. 1. Synthesis and characterization of ionically cross-linked $Ti_3C_2T_x$ MXene. (**A**) Schematic representation of the synthesis of ionically cross-linked $Ti_3C_2T_x$ MXene. (**B**) SEM image of $Ti_3C_2T_x$ (scale bar, 500 nm). (**C**) SEM image of $Ti_3C_2T_x$-PP (scale bar, 2 μm). (**D**) Raman spectra of $Ti_3C_2T_x$, PP, and $Ti_3C_2T_x$-PP. a.u., arbitrary units. (**E**) Representation of the phase change of benzoid PEDOT into quinoid PEDOT.

in-plane vibrations of surface termination —O—, —OH, and —F (*34*). However, the intensity (position) of the $\omega_{1g}(E_g)$ Raman mode was reduced (blue shifted) with cross-linking of PP because of compressive stress on the first several layers of atoms of $Ti_3C_2T_x$; also, surface atoms closely pack, resulting in a blue shift in vibrational wave number (*35*). According to the law of energy relation, there is evidence of enlarged interlayer spacing of MXene because the Raman effect is an inelastic phenomenon. Pristine PP exhibited a prominent peak at 1433 cm^{-1} corresponding to $C\alpha = C\beta$ symmetrical stretching vibration of the five-membered thiophene rings on PEDOT and PEDOT's oxyethylene ring mode at ~988 cm^{-1} (*36*). After cross-linking with $Ti_3C_2T_x$, this peak was red-shifted (~7.47 cm^{-1}) because of the change of PEDOT chains from benzoid to quinoid structure (Fig. 1D), which was interpreted as a relief of the physical restriction of the PEDOT's oxyethylene ring, providing an ability to free vibrations (*36*). PEDOT has two well-known resonant structures: coil phase benzoid and linear or expanded coil phase quinoid in the ground state. The quinoid phase structure causes charge delocalization on PP film and results in enhanced carrier density (*37*–*39*). Eventually, the introduction of PP with $Ti_3C_2T_x$ incited the phase change of the PEDOT chains from benzoid to quinoid structure because of strong π-stacking interactions between PEDOT and the $Ti_3C_2T_x$ basal plane. This intermolecular interaction was also verified by monitoring Raman spectral changes (highlighted with green and red color rectangle boxes) of $Ti_3C_2T_x$ before and after mixing with PP; the band of $Ti_3C_2T_x$ is more sensitive to intermolecular charge transfer. Because of strong noncovalent hydrogen bonding between —O— and —OH termination of $Ti_3C_2T_x$ with $—SO_3H$ and SO_3^- group of PSS, the Raman band (150 to 230 cm^{-1}) corresponding to Ti, C, and O atoms of $Ti_3C_2T_x$ gradually weakened and shifted to higher Raman wave numbers (220 to 270 cm^{-1}) corresponding to Ti, C, O, and H atoms. Thus, the coulombic interaction between PSS and PEDOT led to phase separation between them. Subsequently, PEDOT not only transformed to quinoid phase structure (fig. S2, B and C), but there was also an alignment of linear PEDOT on the surface of $Ti_3C_2T_x$ due to π-π interaction (*40*). The quinoid structure retained PEDOT rings in the same plane (*37*), facilitating π electron delocalization and resulting in an increased conductivity of $Ti_3C_2T_x$-PP. In addition, the attenuated total reflectance Fourier transform infrared (FTIR) spectra (fig. S3; see the Supplementary Materials for details) validated the Raman results. Further, variations in structures, compositions, and surface chemical states of electrode materials of $Ti_3C_2T_x$ and PP and materials after interaction of $Ti_3C_2T_x$ with PP were analyzed by x-ray photoelectron spectroscopy and x-ray diffraction (XRD) patterns, as shown in fig. S4 (see the Supplementary Materials for details). These results indicate that PP was intercalated into the MXene layers and ionically cross-linked with the $Ti_3C_2T_x$ surface.

Fabrication of MXene-based AWIS actuators and assessment of their electrochemical and mechanical properties

For better understanding of the effect of MXene on the actuation performance of AWIS actuators, we prepared flexible ionic actuators

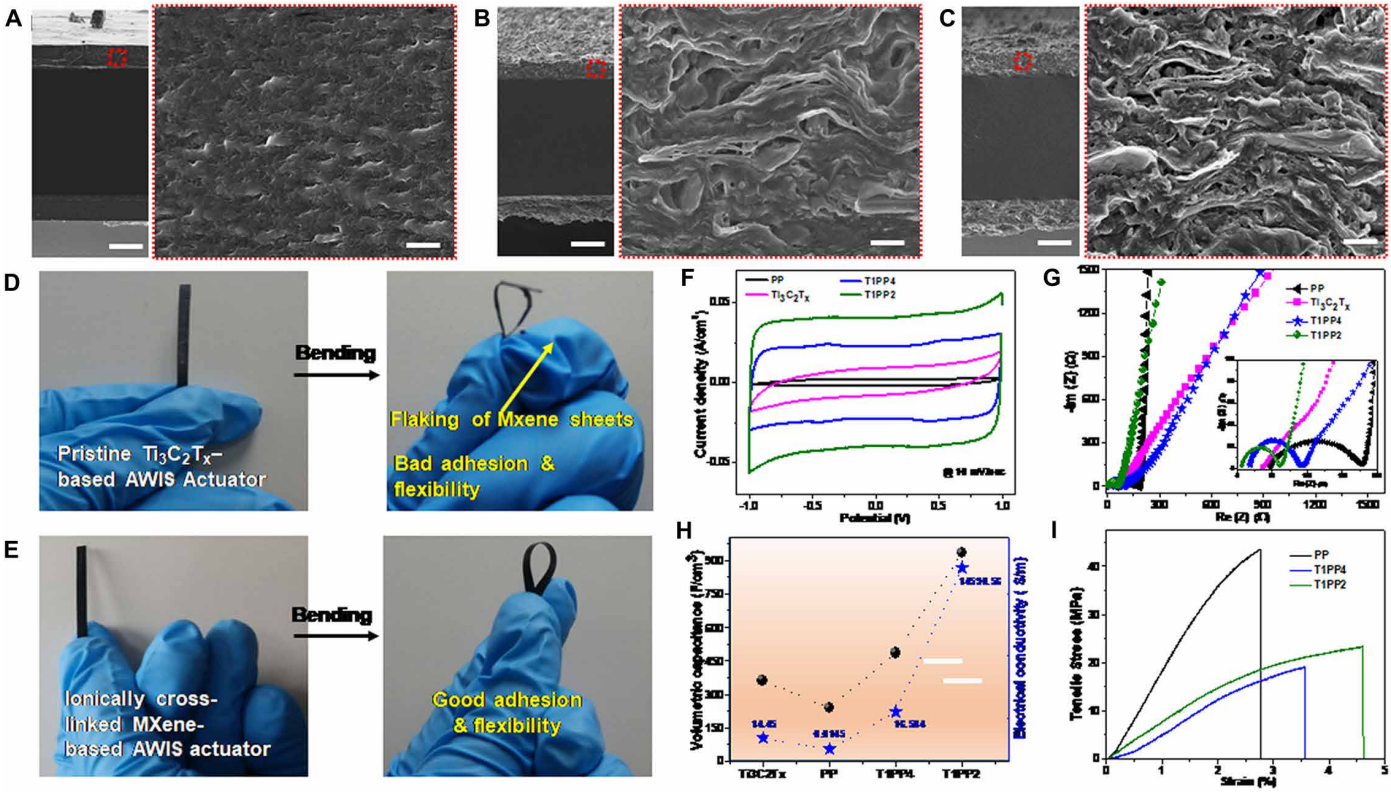

Fig. 2. Morphological, electrical, and electrochemical characterization of all AWIS actuators. (**A** to **C**) Cross-sectional SEM images of PP, T1PP4, and T1PP2 electrodes, respectively. Scale bar, ~15 μm. Insets: SEM images of electrode surface. Scale bars, ~2 μm. (**D**) Optical image of ionic soft actuators with the pristine $Ti_3C_2T_x$ MXene–based electrode, showing flaking of few MXene sheets under bending. (**E**) Optical image of ionic soft actuators with the $Ti_3C_2T_x$-PP–based electrode, indicating good adhesion and flexibility. (**F**) CV curves of four actuators at a scan rate of 10 mV s^{-1}. (**G**) EIS curve of all AWIS actuators. Inset: The magnified high-frequency region. (**H**) The volumetric capacitance value of all AWIS actuators at a scan rate of 10 mV s^{-1} and electrical conductivity of all electrodes. (**I**) Stress-strain curves of PP, T1PP2, and T1PP4 electrode materials.

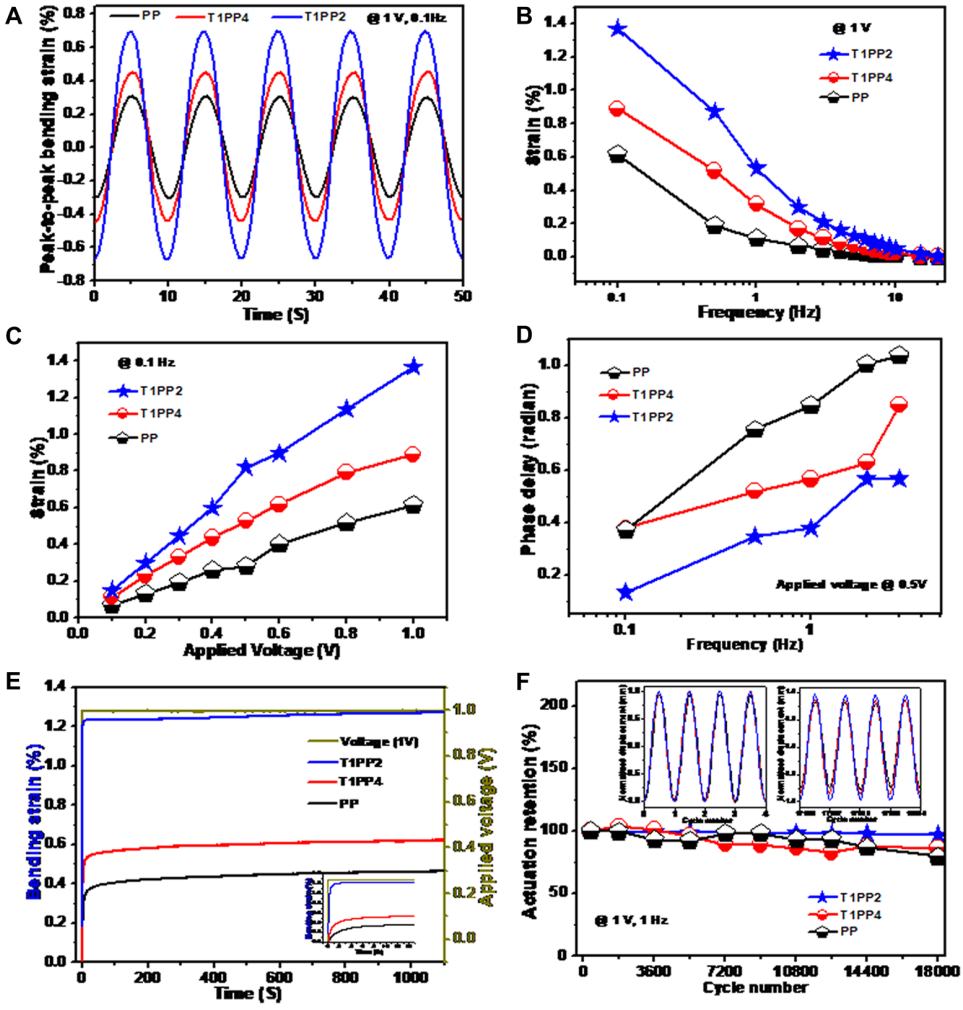

Fig. 3. Actuation performances of AWIS actuators. (**A**) Peak-to-peak bending strain of actuators under sinusoidal input voltage of 1 V at the excitation frequency of 0.1 Hz. (**B**) Peak-to-peak amplitudes of bending strain at a range of frequencies from 0.1 to 20 Hz under sinusoidal input voltage of 1 V. (**C**) Peak-to-peak amplitudes of bending strain with a range of applied voltage from 0.1 to 1 V at 0.1 Hz. (**D**) Phase delay comparison plot of actuator response under sinusoidal input voltage of 0.5 V with varying of frequency from 0.1 to 3 Hz. (**E**) Time-related to actuation performance of AWIS actuators under DC voltage of 0.5 and 1 V. (**F**) Actuation retention test of AWIS actuators for 18,000 cycles under sinusoidal input voltage of 1 V at the excitation frequency of 1 Hz, showing high durability for 5 hours. Inset curves show the first four cycles and the last four cycles of actuation performance.

by drop casting of symmetric electrode material with two different weight ratios of $Ti_3C_2T_x$ to PP [$Ti_3C_2T_x$:PP = 1:4 (T1PP4) and $Ti_3C_2T_x$:PP = 1:2 (T1PP2)]; samples were cut into favorable sizes and shapes (see fig. S5A, and details are in Materials and Methods). Figure 2 (A and C) provides the cross-sectional SEM images of the different actuators. T1PP4 and T1PP2 electrodes had more macroscale porosity than the pristine PP electrode; it seems that PP intercalated between the $Ti_3C_2T_x$ layers. The enhanced porosity will enlarge the accessible surface area of the electrode, which could improve the electrochemical performance with high specific capacitance. The SEM images show the electrode material uniformly coated on the Nafion electrolyte membrane (Nafion membrane containing $EMIm^+$:BF_4^- ionic liquid), with almost identical thickness on both sides. Asymmetric coating of the electrode material on the electrolyte membrane could cause asymmetric actuation due to the high dependency of actuation on the bending stiffness of the actuator. An additional dominant factor in the electrode coating is adhesion with the electrolyte membrane. Weak adhesion leads to flaking of electrode materials, as shown in an image of the pristine MXene electrode (Fig. 2D), and significantly reduces the performance and durability of the actuator. However, strong adhesion between the $Ti_3C_2T_x$-PP electrodes and the electrolyte membrane was established, and no flaking or delamination was observed at the boundary of the two layers, as shown in Fig. 2E. T1PP2 and T1PP4 electrodes show a fractal nature near the edge of the electrolyte membrane, acting as distributed electrode capillaries, which leads to good adhesion between them. The bending displacement of the $Ti_3C_2T_x$-based AWIS actuator is small at 0.1 Hz under low driving voltage (0.5 V), as shown in fig. S6, due to lack of good adhesion and flexibility in comparison to the $Ti_3C_2T_x$-PP–based actuator. It is well known that the capacitance of electrodes directly influences the magnitude of bending deformation and the response time of ionic actuators. Fundamental properties—such as the porosity, hydrophilicity, and chemical affinity of applied electrode materials—are essential, key parameters for the capacitive characteristics of actuators. In this work, to evaluate the energy storage and charge transfer capability, we conducted electrochemical measurements on whole actuator devices and all free electrodes in the ionic liquid electrolyte. For comparison, cyclic voltammogram (CV) of PP, $Ti_3C_2T_x$, and $Ti_3C_2T_x$-PP actuators was measured at the scan rate of 10 mV s^{-1} with an electrochemical window of 2 V, as shown in Fig. 2F. The CV curves display regular rectangular shapes with broad humps, demonstrating excellent capacitive behavior with good ion response (*29*). CV curves of all actuators do not have prominent redox peaks, but pseudocapacitive contribution could not be avoided, indicating that the charge/discharge of actuator electrodes maintains a pseudo-constant rate over the complete voltammetric cycle due to intercalation or electrosorption on the interface surface of the electrode. To elucidate the contribution of the pseudocapacitance, we measured the CV of a free-standing MXene-based electrode using a three-electrode system in ionic liquid electrolyte solution [see fig. S5 (B and C)]. The fractal surface of the electrode at the Nafion interface can be seen in the cross-sectional SEM image of the $Ti_3C_2T_x$-PP actuator; this surface assists the intercalation of the ion inside the electrode. The T1PP2 actuator shows the highest energy storage capability, with a volumetric capacitance of 932 F cm^{-3} at a scan rate of 10 mV s^{-1}, which is nearly four times higher than that of the PP actuator

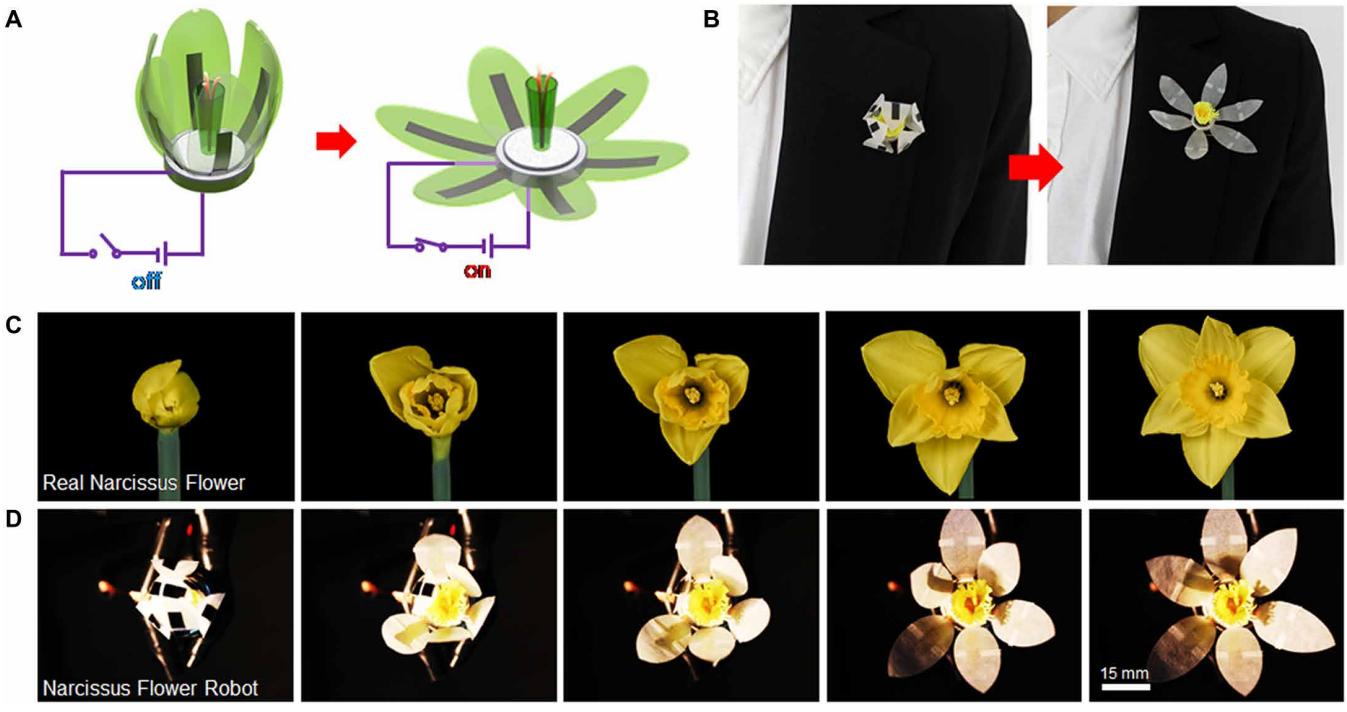

Fig. 4. Demonstration of origami-inspired narcissus flower robot. The total weight of the flower is 375 mg. (**A**) Schematic illustration of the origami-inspired narcissus flower robot: Initially, the robot was in closed position; after applying 3-V DC input, the robot "blooms" like a narcissus flower. (**B**) Optical photographs of the original and the postbloom flower robot, which could serve as a fashion brooch. The flower robot was placed on a black coat worn by our lab secretary J.-Y. Lim. (**C**) Optical images of a real narcissus flower in different stages of blooming taken from www.youtube.com/watch?v=smJmfgaQAR4&t=2s (copyright permission by the owner). (**D**) Optical images of AWIS actuator–based narcissus flower robot in various stages of blooming.

(238 F cm^{-3}); this high value is the result of a sufficient amount of pseudocapacitive $Ti_3C_2T_x$ material loading (*28*). Various previous studies on MXene have examined the restacking tendency between the MXene layers, which inhibits reversible ion and charge transfer to some extent (*32*). Thus, the PP structure can serve as an interactive pillar to prevent restacking of the MXene sheets, to increase the active areas, and to assist in fast reversible electron and ion transport at the interface. Besides this, fig. S5 (E to G) shows CV results at various scan rates from 10 to 500 mV s^{-1}; these were obtained to further realize the capacitance behavior of all actuators due to a direct relation between higher scan rate and higher frequency bandwidth in actuators. Meanwhile, CV curves obtained at a scan rate of 500 mV s^{-1} deviate slightly from the rectangular shape, with a larger broad hump; this is mainly caused by low diffusion of the electrolyte ions under high scan rate. Further, electrochemical impedance spectroscopy (EIS) results support the above arguments. A Nyquist plot of all actuators (Fig. 2G) had a semicircle (high-frequency region) and a straight line (low-frequency region) corresponding to charge-transfer resistance (R_{ct}) and the solid-state diffusion of ions, respectively. The R_{ct} value of the T1PP2 electrode (~54 ohms) is smaller than those of the T1PP4 (>73 ohms) and PP (>130 ohms) electrodes, indicating high charge transport in the T1PP2 electrode, which could contribute to the high capacitance. The series resistance at the high frequency of the T1PP2 electrode is low compared with those of the other electrodes because the incorporation of conduction bands facilitates high electron transport as a result of enhanced electrical conductivity. The electric resistance values of T1PP2 and T1PP4 are lower than those of the neat PP and MXene electrodes. It is confirmed that once the PSS and PEDOT molecules are assembled between the MXene nanosheets, a conductive network is formed via the aligned quinoid phase of PEDOT, maintaining increased interlayer spacing via hindering of layer stacking due to hydrogen bonding between $PSSH/PSS^-$ and $Ti_3C_2T_x$. The resulting fast and high transport of electrons and ions in $Ti_3C_2T_x$-PP is associated with a largely reduced R_{ct} value. The bulk electrical conductivity values of the PP and MXene-based electrodes, as measured by the four-probe method, were calculated to be 14,590.56, 16.504, 14.45, and 0.014466 S cm^{-1} for T1PP2, T1PP4, $Ti_3C_2T_x$, and the pristine PP electrodes, respectively (Fig. 2H). The observed notable improvement in electrical conductivity of the T1PP2 electrode might be due to the modification of the electronic structure of $Ti_3C_2T_x$ via direct ionic cross-linking with PSS and the linearly aligned high conducting quinoid PEDOT phase, which supports the EIS results. In the case of T1PP2, the synergistic effect of $Ti_3C_2T_x$ and the balanced quinoid PEDOT phase content led to high electrical conductivity in comparison with T1PP4. In addition, according to the strain-stress curve (Fig. 2I), the Young's modulus of the T1PP2 electrode is 667.92 MPa, which is smaller than that of the neat PP electrode (1781.45 MPa); however, the strain failure percentage is two times higher than that of PP. Although the tensile strength (23.29 MPa) of T1PP2 is lower than that of the PP electrode, it is significantly higher than that of human skeletal muscle (0.3 MPa) (*1*).

Assessment of actuation performances

With the aim of converting the considerable stored electric energy of MXene-based electrodes into mechanical deformation, we examined the bending deformation of AWIS actuators under different electrical inputs in the open air. Figure 3A shows the peak-to-peak

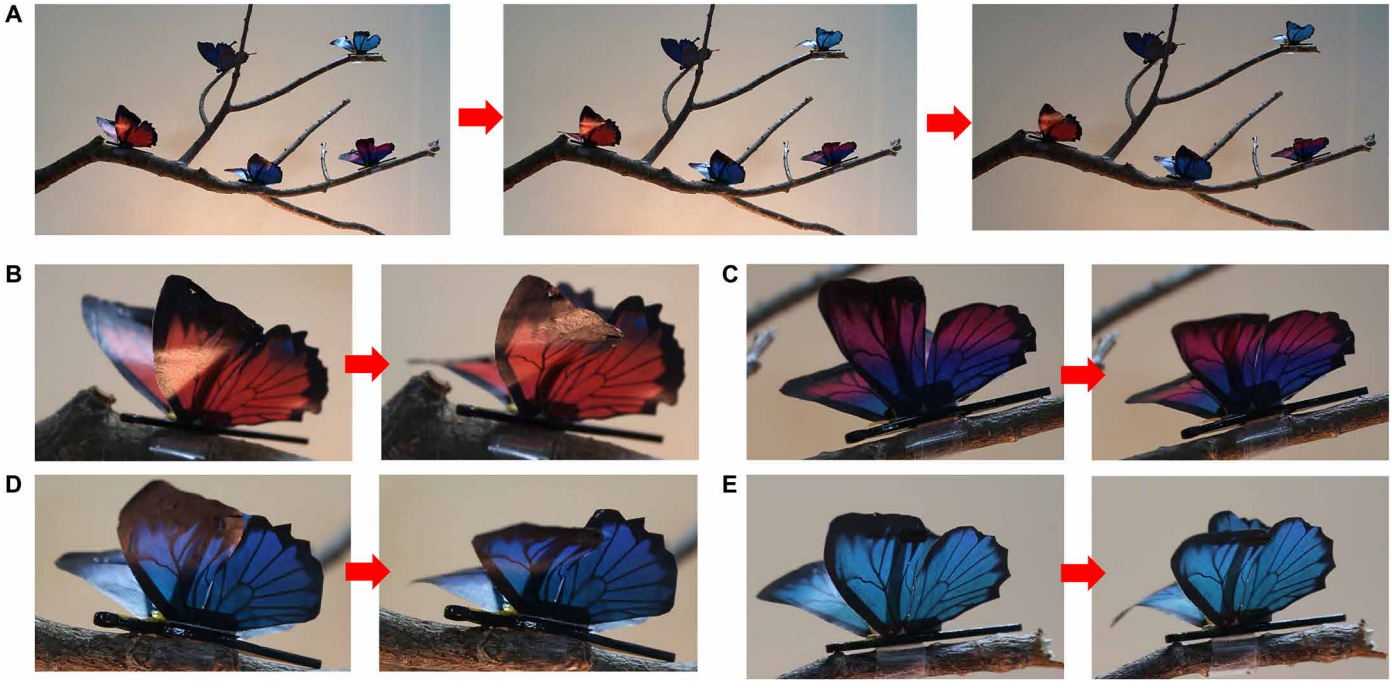

Fig. 5. Demonstration of kinetic art: "Dancing" butterflies on a tree. The weight of each butterfly is 310 mg. (**A** to **E**) Optical images of AWIS actuator–based butterfly robots on tree branches with different wing positions. Initially, the butterflies were in dead position; after applying 2 V of AC input with frequency of 0.2 Hz, butterflies behaved like live butterflies.

bending strains of PP, T1PP4, and T1PP2 ionic actuators under low input voltage (±1 V) at a frequency of 0.1 Hz. Accordingly, the T1PP2 soft actuator exhibited the most bending strain (~1.37%). Figure 3B shows the maximum bending strain of all soft actuators as a function of frequency under harmonic input voltage of 1 V. The AWIS actuators demonstrated a stable frequency response for frequency values up to 20 Hz for all actuators, and the bending strain showed a decreasing profile with an increasing frequency of the driving input. However, the bending strain of the T1PP2 soft actuator is much higher than that of any of the other soft actuators, even at high frequency, whereas the PP soft actuator lost current response at the higher frequency. Therefore, our ionically cross-linked MXene-based AWIS actuators are more favorable for soft actuators that can be operated in a slightly high-frequency range.

According to strain formula $[\varepsilon = \kappa t = 2\delta t/(l^2 + \delta^2)]$, a higher bending actuation strain could be achieved by increasing input voltage, decreasing thickness, and reducing the length of actuators. We evaluated the actuation performances of all three soft actuators under different AC input stimuli and responses. Because of the weakened ion migration rate in actuators under low input voltage, actuation bending strains of all AWIS actuators became smaller with the decreasing voltage to 0.1 V, whereas the T1PP2 soft actuator maintained its high bending performance (~0.15%) even at the low AC input voltage of 0.1 V (Fig. 3C). At 0.3 and 0.2 V, there were notable and comparable bending strains of 0.30 and 0.45%, respectively, in comparison with PP and other carbon-based ionic actuators (*4*, *5*, *18*). The T1PP2 actuator survived under very low voltage from 0.1 to 0.8 V with high frequency up to 20 Hz (fig. S7A). The actuation performance of the T1PP2 actuator was examined with the variable thickness of the Nafion membrane under a harmonic input of 0.5 V at the excitation frequency of 0.1 Hz (fig. S7D). The bending strain linearly decreases as the thickness of the Nafion membrane increases. On the other hand, phase delay was calculated for the frequency range of 0.1 to 3 Hz under the input voltage of 0.5 V, with results shown in Fig. 3D. The phase delay of the T1PP2 soft actuator seems quite small in comparison with those of our neat PP-based actuator, the T1PP4-based actuator, and previously reported graphene-based soft actuators (*5*). This is mainly due to the superior properties of ionically cross-linked transition metal carbide MXene nanomaterials, such as high electrical conductivity, large surface area, high capacitance capability, and flexible molecular structure. Because there was insufficient time for ion diffusion in each period, the phase delay increased with increased excitation frequencies in the electrical input signal.

Furthermore, to precisely investigate the response time, we monitored the bending performance of the soft actuators under the DC voltages of 0.5 and 1 V for 1100 s, with results shown in fig. S7F and Fig. 3E, respectively. The T1PP2 actuator displayed short response time (~1 s) without any sign of back-relaxation compared with those of all other soft actuators (neat PP and T1PP4), graphene/CNT-based actuators, and $BaTiO_3$-based ionic actuators *(7, 41–44)*. These results imply fast charge transfer, much larger charge injection, and fast ion diffusion inside the T1PP2 electrode due to the better conductive path in $Ti_3C_2T_x$ ionically cross-linked with PP. However, a higher PP amount covers most of the MXene sheets in the T1PP4 sample. A large amount of PP not only reduced capacitance but also hindered the charge path, as well as reducing the ion adsorption via low porosity and surface roughness, causing slow response time. Besides this, back-relaxation behavior was noticed to a minimal extent only in the neat PP and T1PP4 AWIS actuators during the DC test under 0.5 V for 1100 s. The back-relaxation was expected to be due to the diffusion effect of water molecules (absorbed from

the open air) in the outer layer because of the hygroscopic nature of PP (*45*). However, in the case of T1PP2, there might not be free PP molecules due to the availability of an appropriate amount of MXene to make ionic bonds. All these properties of the MXene-based electrode in the AWIS actuators are beneficial for high and expedited charge conduction and transfer, ion migration, and energy transduction. The energy transduction efficiency of the actuators is the ratio of the input electric energy to the output mechanical energy (*13*) and is directly proportional to the square of the strain, indicating the higher transduction efficiency of the T1PP2 soft actuator. With regard to the energy efficiency of the actuator, the electrical power consumption is an important consideration. By comparing the power consumption and bending strain of ionic soft actuators reported so far, we found that the MXene-based actuator shows remarkable progress as compared with previously reported actuators as shown in fig. S8. The literature values in fig. S8 were collected from the article written by Kim *et al.* (*6*), which included independent references published during the past 13 years.

According to several previous reports (*13*, *46*), higher ion adsorption in intrinsic graphene actuators may mainly be a result of the capacitance mechanism, which leads to high bending due to the greater expansion of the cathode side. The appearance of MXene, with a unique ionically cross-linked hybrid system, provides an opportunity to improve the performance of next-generation ionic soft actuators. Ionically cross-linked MXene not only has high charge injection, fast charge transportation, and high ion capacity because of its highly conductive path and its high active surface area with abundant pores but also shows better electrochemical and mechanical activity compared with pure PP, pure $Ti_3C_2T_x$-based AWIS, and graphene-based AWIS actuators. The effects of mechanical stiffness and electrical conductivity on the blocking force were investigated. We measured the actuation force of the T1PP2 actuator by applying input voltage from 0.2 to 2 V (fig. S7E). The T1PP2 actuator under the input voltage of 2 V could generate a force 28 times higher than its weight. The T1PP2 actuator showed two times higher blocking force than PP actuators under the very low input voltage of 1 V, as shown in table S2. The comparison data of the actuation force for ionic soft actuators are also presented in table S2.

Ultimately, for the aforementioned practical engineering applications, most soft actuators are required to have not only high bending strain but also cyclic stability and long durability. Thus, the retention performance test of all AWIS actuators was performed for 5 hours with the driving voltage of 1 V and frequency of 1 Hz, with results shown in Fig. 3F. In the case of the PP actuator, the actuation performance was maintained at 80% after 18,000 cycles, but irregular displacement was noticed even after 15,000 cycles (insets of Fig. 3F and fig. S9). However, for the T1PP2 actuator, the first four measured cycles were continually maintained without any distortion at about 97% after 18,000 cycles at 1 Hz (insets of Fig. 3F and fig. S9). The actuation performance of the T1PP4 soft actuator also showed regular displacement after 5 hours, as shown in Fig. 3F and fig. S9. Such high durability benefitted from good adhesion between the electrodes and the polymer electrolyte, together with the prevention of restacking of MXene sheets.

As an interesting application, we applied the MXene-based actuators to make controllable origami structures. A narcissus flower robot with six petals is shown in Fig. 4. The flower was fabricated simply by using MXene AWIS actuators to grasp the middle of paper flower petals (made by laser cutting of weighing paper) with sticky paper wire. The blooming characteristic of the flower was recorded with live snapshots (Fig. 4) as the AWIS actuators worked under a square wave voltage of 3 V. This blooming motion is similar to that of an actual narcissus flower. We used the narcissus flower robot as a brooch on a black coat (Fig. 4B). In addition, butterfly robots on

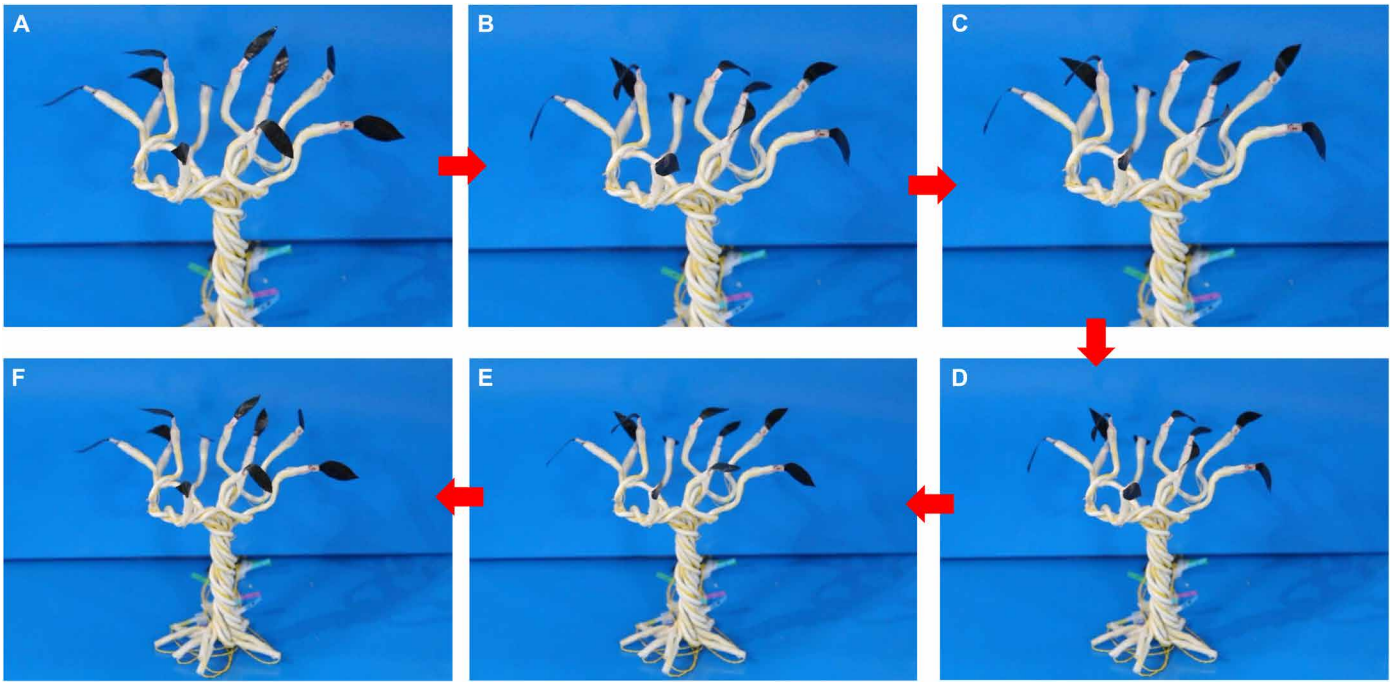

Fig. 6. Demonstration of kinetic art: A tree with dancing leaves. The weight of each leaf is 38 mg. (**A** to **F**) Optical images of AWIS actuator–based kinetic soft sculpture tree with a theme of dancing leaf robot under 1.5-V and 0.2-Hz input stimulation.

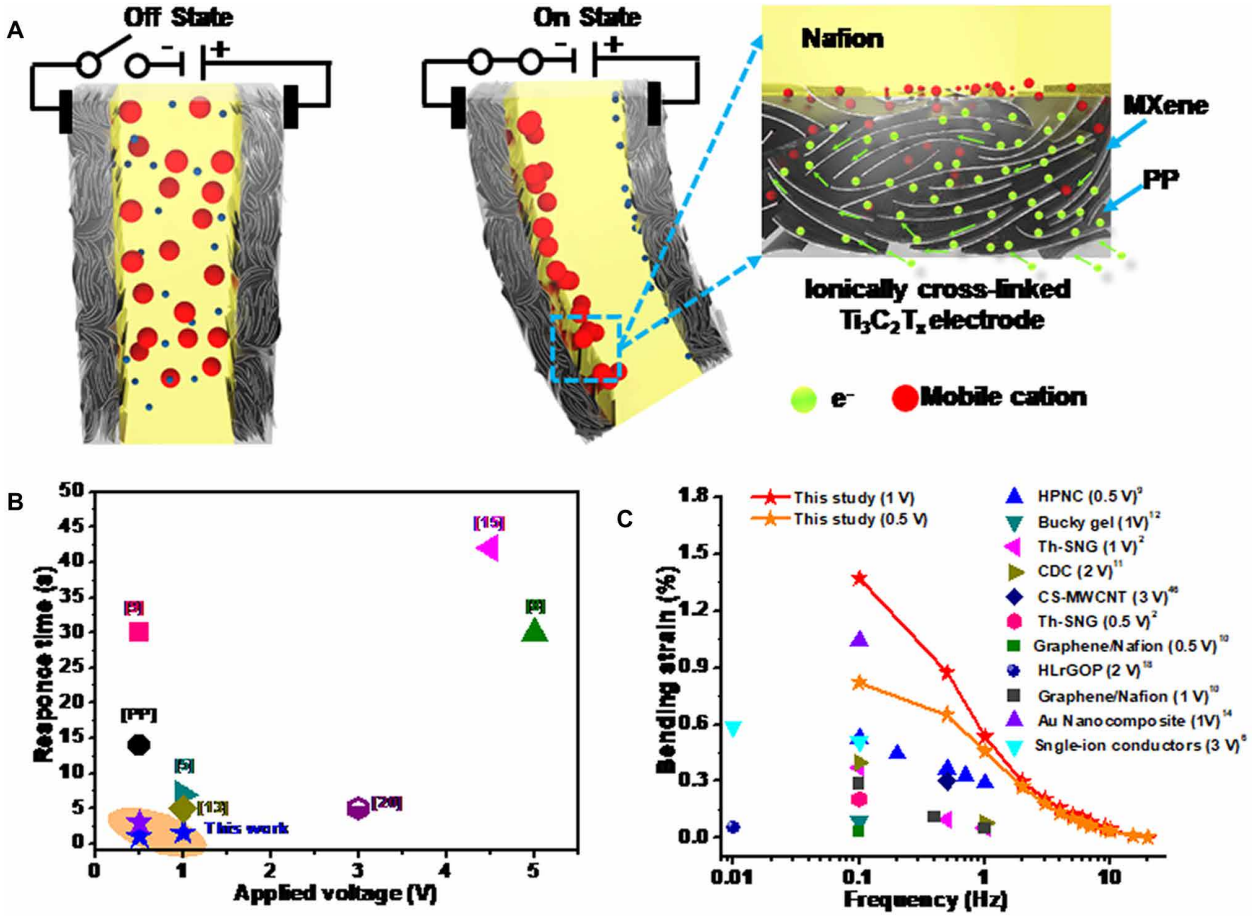

Fig. 7. Schematic analysis of mechanism and performance of MXene AWIS actuators. (**A**) Schematic representation of a mechanism for high and fast actuation of MXene-based AWIS actuators. (**B** and **C**) Visual curves comparing results obtained in this study with results reported in the literature regarding response times and bending strains of ionic soft actuators, respectively.

tree branches with moving wings (Fig. 5) and a kinetic soft sculpture tree with moving leaves (Fig. 6) were demonstrated (movies S2 and S3 and detail discussion in the Supplementary Materials). The implementation for kinetic art may be a promising application in soft robotics because the MXene AWIS actuator has superior bending deformation with very low power consumption. By integrating it with energy harvesting and storage units, this soft robot could be used for both wearable electronics and aesthetic decorations.

DISCUSSION

According to the above results, the MXene artificial muscle shows superior actuation performances due to its high electrical conductivity, ion diffusion ability, and energy storage capability. It was found that the T1PP2 actuator exhibited high bending, and the corresponding maximum peak-to-peak bending strains were up to 551 and 350% higher than those of the neat PP- and T1PP4-based soft actuators, respectively. The larger bending strain was obtained by much higher ion migration and much faster charge transfer via a conducting path formed from the PP ionically bonded to the surface-functionalized $Ti_3C_2T_x$. The actuation mechanism of MXene-based AWIS actuators has been schematically presented in Fig. 7A. First, cations (large ion molecules) and anions (small ion molecules) in the Nafion electrolyte membrane migrated to the cathode and anode sides, respectively, under the applied electric field. Then, cations coordinated with the $Ti_3C_2T_x$-PP structure, leading to an ionically cross-linked transition metal carbide with charge transport from the quinoid phase–aligned PEDOT (more conducting than the benzoid phase of PEDOT) to the conducting MXene surface via the ionically bonded network in the cathode. Besides this highly conductive path, the high porosity and fractal interface area of the electrode and electrolyte membrane, evident in the cross-sectional SEM image (Fig. 2C), can boost the cation adsorption, resulting in improved actuation performance of the ionic soft actuator. Commonly, the arrangement of MXene sheets is mixed between axial and lateral alignment because of the chemical synthesis. Therefore, the electrode of the AWIS actuator will assist cation intercalation on the cathode side under applied electric voltages, resulting in an increased interlayer spacing of the MXene sheets (*28*, *47*). Thus, the $Ti_3C_2T_x$-PP electrode can swell on the cathode side due to increased spacing between the MXene sheets (*41*, *42*), which might aid in the bending of the actuator. The relative volume difference between the two electrodes will induce bending deformations under electrical fields (*42*).

Furthermore, these results indicate the positive effect of MXene in the electrode of the ionic soft actuators, proving that this material can provide a constant conductive path for charge transfer and ion

migration in long-duration functioning. The successful operation of the $Ti_3C_2T_x$-PP–based AWIS actuator for high bending strain at 1 V with a fast response time emphasizes its potential use in a micropower device. The actuation performance of MXene-based AWIS actuators can be considered highly relevant in the framework of electroactive ionic soft actuators, as reported in the most recent literature on AWIS actuators, graphene, bucky gels, CNTs, $BaTiO_3$, Au nanocomposites, and other electroactive ionic chemically modified graphite electrodes (*2*, *4*–*6*, *9*–*12*, *14*, *15*, *18*, *20*, *43*). Visual curves comparing the results obtained in this work with the results reported in the literature concerning electromechanical response time and bending strain of the actuators are shown in Fig. 7 (B and C) and table S3. We found that the ionically cross-linked MXene-based AWIS actuator presented remarkably fast response time compared with other actuators. For the reference of ionic soft actuators, higher bending strains up to about 24 and 35.4% at 1 and 0.5 V, respectively, were observed (Fig. 7C).

In summary, we designed a $Ti_3C_2T_x$ MXene electrode ionically cross-linked with PP for high-performance AWIS artificial muscles. This ionically cross-linked MXene electrode-based actuators exhibited high bending strains of 1.37% under sinusoidal input voltage of 1 V with the frequency of 0.1 Hz and ultrafast actuation response within 1 s without back-relaxation under DC input signals. The MXene-based actuators retained high durability over ~5 hours, without any distortion or delamination of the electrode, at 1-Hz frequency. Applications of highly conductive MXene-based AWIS actuators with high bending strain under ultralow driving voltage emphasize the enormous potential in the field of smart, flexible components including soft robotics, biomimetic robots, haptic feedback systems, and biomedical devices. As a result, an origami-inspired narcissus flower robot, dancing leaves, and butterfly robots made with the MXene soft actuators showed controllable and repeatable blooming, demonstrating its possibility as a wearable kinetic decoration product on clothes. This study confirmed that actuators based on ionically cross-linked MXene enable successful robotic operation under low input voltages, thus paving the way for more advanced biomimetic technologies based on micropower devices in the future.

MATERIALS AND METHODS

Preparation of ionically cross-linked $Ti_3C_2T_x$ MXene electrode material

MAX powder (Ti_3AlC_2) was used as the precursor to fabricate $Ti_3C_2T_x$ MXene. To synthesize $Ti_3C_2T_x$, we added 40 ml of 9 M HCl (Sigma-Aldrich) to 2 g of LiF (Alfa Aesar) under mild stirring to dissolve the salt. After that, 1 g of Ti_3AlC_2 powder was added slowly to the mixed solution under an ice bath. The reaction mixture was retained at 34°C for 12 hours. The mixture was washed 10 times by adding deionized water and shaking for 1 min after each washing, along with centrifugation at 3500 rpm for 5 min for each cycle; mixtures were then decanted. After the final centrifugation, the sediment of the MXene semi-solution was filtered via vacuum-assisted filtration and collected, resulting in MXene powders.

Ionically cross-linked $Ti_3C_2T_x$ MXene electrode material was synthesized by a one-step reaction of PP and $Ti_3C_2T_x$ MXene in *N*,*N*′-dimethylformamide (DMF) at room temperature for 6 hours at the ambient temperature. T1PP2 and T1PP4 were obtained by changing the weight % of PP suspension with 2 and 4, respectively. For comparison, we used pure PP and MXene solutions.

Fabrication of ionically cross-linked $Ti_3C_2T_x$ MXene AWIS actuator

The ionic polymer membrane was prepared to direct the cast of the Nafion-ionic liquid solution on a glass petri dish; the sample was then dried at 90°C for 6 hours. In detail, 1 g of Nafion was dissolved in 20 ml dimethylacetamide at 60°C, followed by adding 0.6 g of $EMImBF_4$ and stirring for 24 hours at 45°C to make a homogeneous solution. After that, 5 ml of solution was cast on a glass petri dish to obtain a 110-μm-thick membrane. To prepare a layer-by-layer sandwiched structure, MXene-based ionic actuators were fabricated by direct coating of the mixture of electrode materials (PP, $Ti_3C_2T_x$, T1PP2, and T1PP4) with DMF on both sides of a Nafion membrane, merely using a dropper; samples were then dried at 90°C for 40 min. Last, for further actuation testing, each of the ionic soft actuators was cut to a free length of 10 mm and width of 3 mm.

Characterization techniques

The surface morphologies of the MXene, PP, and ionically cross-linked MXene structures were observed by field emission TEM (Tecnai F20, FEI) and field emission SEM (Nova230, FEI). The chemical composition and structure of all electrode materials were analyzed using x-ray photoelectron spectroscopy (K-Alpha, Thermo VG Scientific), XRD (Rigaku D/MAX-2500 with CuKα radiation), and FTIR (Nicolet iS50, Thermo Fisher Scientific Instrument). The surface resistance of the graphene meshes was measured using a four-probe measurement system (Keithley Multimeter DMM7510).

Electrochemical measurements and actuation test

All electrochemical characterizations of the actuators were recorded by a multichannel potentiostat/galvanostat (VersaSTAT, Princeton Applied Research). Volumetric capacitance (*C*) values were calculated at various scan rates from 10 to 100 mV s^{-1}, using Eq. 1

$$C = \frac{1}{\Delta V s v}\int_{V_1}^{V_2} I \Delta V \quad (1)$$

Here, ΔV is the potential window, *s* is the scan rate, and *v* refers to the volume of the actuator. EIS over a frequency range of 0.01 to 100 KHz was conducted by applying a sinusoidal signal of 50-mV amplitude. A probe station (MSTech, model 4000) was used to measure the sheet resistance of the flexible electrode. A table-top universal testing machine (AGS X; Shimadzu Corp., Japan) was used to measure the mechanical properties of the electrodes. The maximum displacement of all actuators was determined using a National Instrument PCI eXtensions for Instrumentation data acquisition system (NI-PXI1042Q and NI-PXI 6252 board) and a current amplifier (UPM1504). The maximum displacement (δ) of the actuator was measured by a laser displacement sensor (LK-031, Keyence), where the bending strain (ε) and curvature (κ) were estimated according to Eq. 2 (*44*)

$$\varepsilon = \kappa t = \frac{2\delta t}{l^2 + \delta^2} \quad (2)$$

where *t*, δ, and *l* are the thickness, the displacement, and the free length of the actuator, respectively.

The phase delay (Δφ) was calculated using Eq. 3

$$\Delta\varphi = 2\pi f \Delta t \quad (3)$$

where Δt refers to the time delay and f represents the frequency of signal, which can be calculated using the time difference between two equivalent points of the signals. Energy density (E_d), power density (P_d), and the efficiency of the electrical to mechanical energy conversion (transduction efficiency ~ $\eta_{transduction}$) were estimated by the following equations (*44*, *48*)

$$E_d = \frac{\gamma\varepsilon^2}{2}, P_d = 2f\gamma\varepsilon^2, \text{and } \eta_{transduction} = \frac{0.5\,\gamma\varepsilon^2 f\,\text{vol.}}{V.I} \quad (4)$$

where γ is the Young's modulus of the actuator, f is driving frequency of the applied voltage, ε is the bending strain of actuator, vol. is the volume of the whole actuator, and $V.I$ is the electric power consumption. The material properties of actuators are listed in table S1.

SUPPLEMENTARY MATERIALS

robotics.sciencemag.org/cgi/content/full/4/33/eaaw7797/DC1
Fig. S1. Schematic representation for synthesis of $Ti_3C_2T_x$ and morphological images.
Fig. S2. Ionically cross-linked MXene-PP electrode.
Fig. S3. FTIR spectra of all MXene materials.
Fig. S4. Chemical and structural characterization of all AWIS actuator electrodes.
Fig. S5. Fabrication of actuators and electrochemical CV results.
Fig. S6. Actuation performance of neat $Ti_3C_2T_x$ MXene–based ionic soft actuator under various input voltages at a frequency of 0.1 Hz.
Fig. S7. Actuation performances of T1PP2 and T1PP4 AWIS actuators.
Fig. S8. Comparison graph for power consumption–strain dependency of MXene-based actuator compared with other soft actuators.
Fig. S9. Durability results of all actuators.
Table S1. Mechanical properties of PP, T1PP4, and T1PP2 electrodes.
Table S2. Comparison of blocking force for ionic soft actuators.
Table S3. Comparison of bending strain for ionic soft actuators.
Movie S1. Kinetic art demonstration of origami-inspired narcissus flower robot.
Movie S2. Kinetic art demonstration of dancing butterfly robots.
Movie S3. Kinetic art demonstration of dancing leaves.
References (*49*–*52*)

REFERENCES AND NOTES

1. R. H. Baughman, Playing nature's game with artificial muscles. *Science* **308**, 63–65 (2005).
2. M. Kotal, J. Kim, K. J. Kim, I.-K. Oh, Sulfur and nitrogen co-doped graphene electrodes for high-performance ionic artificial muscles. *Adv. Mater.* **28**, 1610–1615 (2016).
3. V. H. Nguyen, J. Kim, R. Tabassian, M. Kotal, K. Jun, J. H. Oh, J. M. Son, M. T. Manzoor, K. J. Kim, I. K. Oh, Electroactive artificial muscles based on functionally antagonistic core–shell polymer electrolyte derived from PS-*b*-PSS block copolymer. *Adv. Sci.* **6**, 1801196 (2018).
4. M. Kotal, J. Kim, R. Tabassian, S. Roy, V. H. Nguyen, N. Koratkar, I. K. Oh, Highly bendable ionic soft actuator based on nitrogen-enriched 3D hetero-nanostructure electrode. *Adv. Funct. Mater.* **28**, 1802464 (2018).
5. R. Tabassian, J. Kim, V. H. Nguyen, M. Kotal, I.-K. Oh, Functionally antagonistic hybrid electrode with hollow tubular graphene mesh and nitrogen-doped crumpled graphene for high-performance ionic soft actuators. *Adv. Funct. Mater.* **28**, 1705714 (2018).
6. O. Kim, H. Kim, U. H. Choi, M. J. Park, One-volt-driven superfast polymer actuators based on single-ion conductors. *Nat. Commun.* **7**, 13576 (2016).
7. J.-H. Lee, J.-D. Nam, H. R. Choi, H. M. Kim, J. W. Jeon, Water uptake and migration effect on IPMC(ion-exchange polymer metal composite) actuator, in Proceedings of SPIE—The International Society for Optical Engineering, Smart Structures and Materials 2001:Electroactive Polymer Actuators and Devices, Newport Beach, 5 to 8 March 2011, vol. 4329, pp. 84–92.
8. A. Khan, R. K. Jain, P. Banerjee, B. Ghosh, Inamuddin, A. M. Asiri, Development, characterization and electromechanical actuation behavior of ionic polymer metal composite actuator based on sulfonated poly(1,4-phenylene ether-ether-sulfone)/carbon nanotubes. *Sci. Rep.* **8**, 9909 (2018).
9. S. Roy, J. Kim, M. Kotal, K. J. Kim, I.-K. Oh, Artificial muscles: Electroionic antagonistic muscles based on nitrogen-doped carbons derived from poly(triazine-triptycene). *Adv. Sci.* **4**, 1770062 (2017).
10. J.-H. Jung, J.-H. Jeon, V. Sridhar, I.-K. Oh, Electro-active graphene—Nafion actuators. *Carbon* **49**, 1279–1289 (2011).
11. J. Torop, V. Palmre, M. Arulepp, T. Sugino, K. Asaka, A. Aabloo, Flexible supercapacitor-like actuator with carbide-derived carbon electrodes. *Carbon* **49**, 3113–3119 (2011).
12. T. Fukushima, K. Asaka, A. Kosaka, T. Aida, Fully plastic actuator through layer-by-layer casting with ionic-liquid-based bucky gel. *Angew. Chem. Int. Ed.* **44**, 2410–2413 (2005).
13. L. Kong, W. Chen, Carbon nanotube and graphene-based bioinspired electrochemical actuators. *Adv. Mater.* **26**, 1025–1043 (2014).
14. Y. Yan, T. Santaniello, L. G. Bettini, C. Minnai, A. Bellacicca, R. Porotti, I. Denti, G. Faraone, M. Merlini, C. Lenardi, P. Milani, Electroactive ionic soft actuators with monolithically integrated gold nanocomposite electrodes. *Adv. Mater.* **29**, 1606109 (2017).
15. D. Nevstrueva, K. Murashko, V. Vunder, A. Aabloo, A. Pihlajamäki, M. Mänttäri, J. Pyrhönen, T. Koiranen, J. Torop, Natural cellulose ionogels for soft artificial muscles. *Colloids Surf. B Biointerfaces* **161**, 244–251 (2018).
16. C. Lu, Y. Yang, J. Wang, R. Fu, X. Zhao, L. Zhao, Y. Ming, Y. Hu, H. Lin, X. Tao, Y. Li, W. Chen, High-performance graphdiyne-based electrochemical actuators. *Nat. Commun.* **9**, 752 (2018).
17. J. Torop, M. Arulepp, T. Sugino, K. Asaka, A. Jänes, E. Lust, A. Aabloo, Microporous and mesoporous carbide-derived carbons for strain modification of electromechanical actuators. *Langmuir* **30**, 2583–2587 (2014).
18. J. Kim, J.-H. Jeon, H.-J. Kim, H. Lim, I.-K. Oh, Durable and water-floatable ionic polymer actuator with hydrophobic and asymmetrically laser-scribed reduced graphene oxide paper electrodes. *ACS Nano* **8**, 2986–2997 (2014).
19. J. Ru, Z. Zhu, Y. Wang, H. Chen, D. Li, Tunable actuation behavior of ionic polymer metal composite utilizing carboxylated carbon nanotube-doped Nafion matrix. *RSC Adv.* **8**, 3090–3094 (2018).
20. K. Bian, H. Liu, G. Tai, K. Zhu, K. Xiong, Enhanced actuation response of Nafion-based ionic polymer metal composites by doping $BaTiO_3$ nanoparticles. *J. Phys. Chem. C* **120**, 12377–12384 (2016).
21. K. Mukai, K. Asaka, T. Sugino, K. Kiyohara, I. Takeuchi, N. Terasawa, D. N. Futaba, K. Hata, T. Fukushima, T. Aida, Highly conductive sheets from millimeter-long single-walled carbon nanotubes and ionic liquids: Application to fast-moving, low-voltage electromechanical actuators operable in air. *Adv. Mater.* **21**, 1582–1585 (2009).
22. T. Terse-Thakoor, K. Komori, P. Ramnani, I. Lee, A. Mulchandani, Electrochemically functionalized seamless three-dimensional graphene-carbon nanotube hybrid for direct electron transfer of glucose oxidase and bioelectrocatalysis. *Langmuir* **31**, 13054–13061 (2015).
23. M. Naguib, V. N. Mochalin, M. W. Barsoum, Y. Gogotsi, 25th anniversary article: MXenes: A new family of two-dimensional materials. *Adv. Mater.* **26**, 992–1005 (2014).
24. L. Qin, Q. Tao, A. El Ghazaly, J. Fernandez-Rodriguez, P. O. Å. Persson, J. Rosen, F. Zhang, High-performance ultrathin flexible solid-state supercapacitors based on solution processable $Mo_{1.33}C$ MXene and PEDOT:PSS. *Adv. Funct. Mater.* **28**, 1703808 (2017).
25. S. Niu, Z. Wang, M. Yu, M. Yu, L. Xiu, S. Wang, X. Wu, J. Qiu, MXene-based electrode with enhanced pseudocapacitance and volumetric capacity for power-type and ultra-long life lithium storage. *ACS Nano* **12**, 3928–3937 (2018).
26. Y. Yang, S. Umrao, S. Lai, S. Lee, Large-area highly conductive transparent two-dimensional Ti_2CT_x film. *J. Phys. Chem. Lett.* **8**, 859–865 (2017).
27. F. Shahzad, M. Alhabeb, C. B. Hatter, B. Anasori, S. M. Hong, C. M. Koo, Y. Gogotsi, Electromagnetic interference shielding with 2D transition metal carbides (MXenes). *Science* **353**, 1137–1140 (2016).
28. J. Come, J. M. Black, M. R. Lukatskaya, M. Naguib, M. Beidaghi, A. J. Rondinone, S. V. Kalinin, D. J. Wesolowski, Y. Gogotsi, N. Balke, Controlling the actuation properties of MXene paper electrodes upon cation intercalation. *Nano Energy* **17**, 27–35 (2015).
29. M. Boota, B. Anasori, C. Voigt, M.-Q. Zhao, M. W. Barsoum, Y. Gogotsi, Pseudocapacitive electrodes produced by oxidant-free polymerization of pyrrole between the layers of 2D titanium carbide (MXene). *Adv. Mater.* **28**, 1517–1522 (2018).
30. C. Eames, M. S. Islam, Ion intercalation into two-dimensional transition-metal carbides: Global screening for new high-capacity battery materials. *J. Am. Chem. Soc.* **136**, 16270–16276 (2014).
31. Z. Ling, C. E. Ren, M.-Q. Zhao, J. Yang, J. M. Giammarco, J. Qiu, M. W. Barsoum, Y. Gogotsi, Flexible and conductive MXene films and nanocomposites with high capacitance. *Proc. Natl. Acad. Sci. U.S.A.* **111**, 16676–16681 (2014).
32. M. Zhu, Y. Huang, Q. Deng, J. Zhou, Z. Pei, Q. Xue, Y. Huang, Z. Wang, H. Li, Q. Huang, C. Zhi, Highly flexible, freestanding supercapacitor electrode with enhanced performance obtained by hybridizing polypyrrole chains with MXene. *Adv. Energy Mater.* **6**, 1600969 (2016).
33. Y. Li, R. Tanigawa, H. Okuzaki, Soft and flexible PEDOT/PSS films for applications to soft actuators. *Smart Mater. Struct.* **23**, 074010 (2014).
34. T. Hu, J. Wang, H. Zhang, Z. Li, M. Hu, X. Wang, Vibrational properties of Ti_3C_2 and $Ti_3C_2T_2$ (T = O, F, OH) monosheets by first-principles calculations: A comparative study. *Phys. Chem. Chem. Phys.* **17**, 9997–10003 (2015).
35. C. Y. Xu, P. X. Zhang, L. Yan, Blue shift of Raman peak from coated TiO_2 nanoparticles. *J. Raman Spectrosc.* **32**, 862–865 (2001).
36. S. Funda, T. Ohki, Q. Liu, J. Hossain, Y. Ishimaru, K. Ueno, H. Shirai, Correlation between the fine structure of spin-coated PEDOT:PSS and the photovoltaic performance of organic/crystalline-silicon heterojunction solar cells. *J. Appl. Phys.* **120**, 33103 (2016).

37. J. Zhou, G. Lubineau, Improving electrical conductivity in polycarbonate nanocomposites using highly conductive PEDOT/PSS coated MWCNTs. *ACS Appl. Mater. Interfaces* **5**, 6189–6200 (2013).
38. J. J. Lee, S. H. Lee, F. S. Kim, H. H. Choi, J. H. Kim, Simultaneous enhancement of the efficiency and stability of organic solar cells using PEDOT:PSS grafted with a PEGME buffer layer. *Org. Electron.* **26**, 191–199 (2015).
39. A. A. Farah, S. A. Rutledge, A. Schaarschmidt, R. Lai, J. P. Freedman, A. S. Helmy, Conductivity enhancement of poly(3,4-ethylenedioxythiophene)-poly(styrenesulfonate) films post-spincasting. *J. Appl. Phys.* **112**, 113709 (2012).
40. S. Tu, Q. Jiang, X. Zhang, H. N. Alshareef, Large dielectric constant enhancement in MXene percolative polymer composites. *ACS Nano* **12**, 3369–3377 (2018).
41. Y. Dall'Agnese, P. Rozier, P.-L. Taberna, Y. Gogotsi, P. Simon, Capacitance of two-dimensional titanium carbide (MXene) and MXene/carbon nanotube composites in organic electrolytes. *J. Power Sources* **306**, 510–515 (2016).
42. N. Jäckel, B. Krüner, K. L. van Aken, M. Alhabeb, B. Anasori, F. Kaasik, Y. Gogotsi, V. Presser, Electrochemical in situ tracking of volumetric changes in two-dimensional metal carbides (MXenes) in ionic liquids. *ACS Appl. Mater. Interfaces* **8**, 32089–32093 (2016).
43. L. Lu, W. Chen, Biocompatible composite actuator: A supramolecular structure consisting of the biopolymer chitosan, carbon nanotubes, and an ionic liquid. *Adv. Mater.* **22**, 3745–3748 (2010).
44. P.-J. Cottinet, C. Souders, D. Labrador, S. Porter, Z. Liang, B. Wang, C. Zhang, Nonlinear strain–electric field relationship of carbon nanotube buckypaper/Nafion actuators. *Sens. Actuators A Phys.* **170**, 164–171 (2011).
45. A.-B. Sun, D. Bajon, J.-M. Moschetta, E. Benard, C. Thipyopas, Integrated static and dynamic modeling of an ionic polymer–metal composite actuator. *J. Intell. Mater. Syst. Struct.* **26**, 1164–1178 (2015).
46. S. Liu, Y. Liu, H. Cebeci, Roberto Guzman de Villoria, J.-H. Lin, B. L. Wardle, Q. Zhang, Conductive filler morphology effect on performance of ionic polymer conductive network composite actuators, in *Electroactive Polymer Actuators and devices (EAPAD)*, Y. Bar-Cohen, Ed. (SPIE, 2010), vol. 764219; http://proceedings.spiedigitallibrary.org/proceeding.aspx?doi=10.1117/12.847619.
47. Z. Lin, P. Rozier, B. Duployer, P. L. Taberna, B. Anasori, Y. Gogotsi, P. Simon, Electrochemical and in-situ X-ray diffraction studies of $Ti_3C_2T_x$ MXene in ionic liquid electrolyte. *Electrochem. Commun.* **72**, 50–53 (2016).
48. O. Kim, T. J. Shin, M. J. Park, Fast low-voltage electroactive actuators using nanostructured polymer electrolytes. *Nat. Commun.* **4**, 2208 (2013).
49. G. Wu, Y. Hu, Y. Liu, J. Zhao, X. Chen, V. Whoehling, C. Plesse, G. T. M. Nguyen, F. Vidal, W. Chen, Graphitic carbon nitride nanosheet electrode-based high-performance ionic actuator. *Nat. Commun.* **6**, 7258 (2015).
50. S. Roy, J. Kim, M. Kotal, R. Tabassian, K. J. Kim, I.-K. Oh, Collectively exhaustive electrodes based on covalent organic framework and antagonistic co-doping for electroactive ionic artificial muscles. *Adv. Funct. Mater.* **29**, 1900161 (2019).
51. J. Kim, S.-H. Bae, M. Kotal, T. Stalbaum, K. J. Kim, I.-K. Oh, Soft but powerful artificial muscles based on 3D graphene–CNT–Ni heteronanostructures. *Small* **13**, 1701314 (2017).
52. T. Sugino, K. Kiyohara, I. Takeuchi, K. Mukai, K. Asaka, Actuator properties of the complexes composed by carbon nanotube and ionic liquid: The effects of additives. *Sens. Actuators B* **141**, 179–186 (2009).

Acknowledgments: We thank J.-Y. Lim for dressing up in a black coat to demonstrate the flower robotic brooch. **Funding:** This work was supported by the Creative Research Initiative Program (2015R1A3A2028975) funded by the National Research Foundation of Korea (NRF). S.U. acknowledges the partial financial support from the NRF fund (NRF-2017R1D1A1B03029402) for fabrication of MXene samples. **Author contributions:** S.U. and I.-K.O. conceived the idea of MXene-based ionic soft actuators. S.U. carried out the whole experiments, analyzed the data, and wrote the draft of the manuscript. J.K. helped to fabricate the actuator and to measure the actuation performance. R.T., V.H.N., and Q.Z. also contributed to testing actuators and to preparing a robotic model. I.-K.O. supervised the research at all stages, led all groups, and wrote the manuscript. All the authors discussed the results and commented on the manuscript. **Competing interests:** The authors declare that they have no competing financial interests. **Data and materials availability:** All data needed to evaluate the conclusions in the paper are present in the paper or the Supplementary Materials.

Submitted 24 January 2019
Accepted 23 July 2019
Published 21 August 2019
10.1126/scirobotics.aaw7797

Citation: S. Umrao, R. Tabassian, J. Kim, V. H. Nguyen, Q. Zhou, S. Nam, I.-K. Oh, MXene artificial muscles based on ionically cross-linked $Ti_3C_2T_x$ electrode for kinetic soft robotics. *Sci. Robot.* **4**, eaaw7797 (2019).

Science Robotics

MXene artificial muscles based on ionically cross-linked $Ti_3C_2T_x$ electrode for kinetic soft robotics

Sima Umrao, Rassoul Tabassian, Jaehwan Kim, Van Hiep Nguyen, Qitao Zhou, Sanghee Nam, and Il-Kwon Oh

Sci. Robot. **4** (33), eaaw7797. DOI: 10.1126/scirobotics.aaw7797

Science Robotics (ISSN 2470-9476) is published by the American Association for the Advancement of Science. 1200 New York Avenue NW, Washington, DC 20005. The title *Science Robotics* is a registered trademark of AAAS.